QUALIFICATION OF TI6AL4V ELI ALLOY PRODUCED BY LASER POWDER BED FUSION FOR BIOMEDICAL APPLICATIONS

I. Yadroitsev*, P. Krakhmalev**, I. Yadroitsava*, and A. Du Plessis***

* Department of Mechanical and Mechatronic Engineering, Bloemfontein, Central University of Technology, Free State, South Africa, 9300
** Department of Engineering and Physics, Karlstad University, Sweden, 651 88
*** University of Stellenbosch, Private Bag X1, Matieland, Stellenbosch, South Africa, 7602

Abstract

Ti6Al4V ELI samples were manufactured by Laser Powder Bed Fusion (LPBF) in vertical and horizontal directions and subjected to various heat treatments. Detailed analyses of porosity, microstructure, residual stress, tensile properties, fatigue and fractured surfaces were performed based on X-ray micro computed tomography, scanning electron microscopy and X-ray diffraction methods. Types of fractures and tensile fracture mechanisms in LPBF Ti6Al4V ELI alloy were studied. Detailed analysis of the microstructure and the corresponding mechanical properties were compared with standard specifications for conventional Ti6Al4V alloy (grade 5 and 23) for surgical implant applications. Conclusions regarding mechanical properties and heat treatment of LPBF Ti6Al4V ELI for biomedical applications were made.

Introduction

Biocompatibility and low density of Ti6Al4V alloy are the decisive factors for biomedical applications such as implants. Strength, corrosion resistance, low specific weight ensure wide application of Ti6Al4V for high-performance engineering solutions in high-tech industry.

Additive Manufacturing represents a new manufacturing paradigm. These technologies are unique and have the potential to radically change manufacturing as we know it. Laser Powder Bed Fusion (LPBF) or Direct Metal Laser Sintering is an important part of this class technologies and gives new opportunities to work with metal materials. Complexity, variety, time, possibility of using different material in one-cycle manufacturing, and less waste, because only the material that is needed is used, are main and real benefits of LPBF.

A 3D LPBF object consists on a basic level of single tracks and layers having metallurgical contacts. Under different process parameters, the single tracks can be stable or unstable, resulting in a variability in geometrical size across the object. For example, for a fixed scanning speed and powder layer thickness, when the laser power is changed from 100 to 200 W, the balling effect can start or very deep penetration occurs (Figure 1). Keyhole mode or balling effect leads to high porosity and consequently deterioration of mechanical properties. Optimal and stable process-parameters are therefore a prerequisite for high-quality LPBF products (Yadroitsev *et al.,* 2015).

Under laser melting/solidification/heating processes, columnar grains of β-phase grow through track's and layer's boundaries in Ti6Al4V alloy. The microstructure of LPBF alloy is a result of rapid solidification, which differs completely from cast/wrought material since the cooling

rate at LPBF is very high (about 10^6 K/s). High cooling rates promote the formation of the acicular/lamellar α′ *hcp* martensitic phase in Ti6Al4V alloy. LPBF material has higher strength but is inherently less ductile than the globular microstructure formed during conventional processing (Kasperovich and Hausmann, 2015). Different process parameters and scanning strategies influence the microstructure and hence the mechanical properties. For wide applications in medical industry it is crucially important that LPBF Ti6Al4V ELI implants comply with international standards regarding microstructure and mechanical properties.

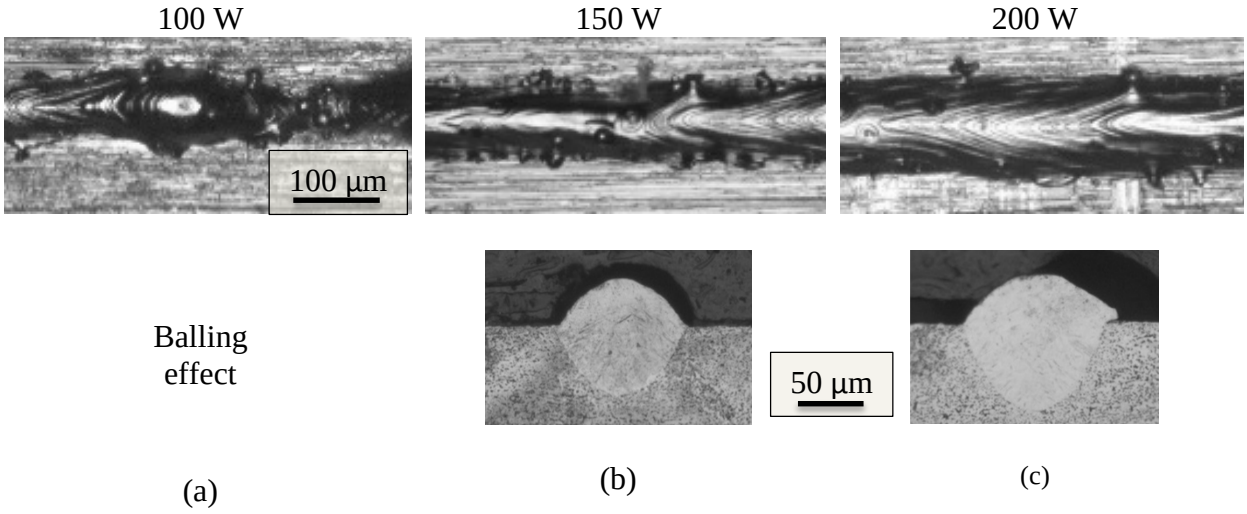

Figure 1. Top view and cross-sections of Ti6Al4V ELI tracks at different laser power: 100 W (a), 150 W (b) and 200 W (c). Powder layer thickness is about 50 μm, laser spot size is 80 μm, and scanning speed of 1.4 m/s.

Chemical composition requirements for additive manufactured alloys coincide with conventional materials (Table 1). Mechanical properties of conventional cast and wrought Ti6Al4V material and appropriate heat treatments and processing are well-documented in standards for biomedical applications (ASTM standards F1108–14, F147208, F136–13, F620–11, ISO standard 20160:2006). For Ti6Al4V produced by powder bed fusion, ASTM standards F2924 and F3001-14 assume quite variable elongation of 6-10%. Minimum tensile properties for Ti6Al4V ELI alloy are similar to wrought annealed material for surgical implants (Figure 2).

Table 1 Chemical composition for grade 5 (Ti6Al4V) and grade 23 (Ti6Al4V ELI) alloys required for surgical implants

N	C	H	Fe	O	Al	V	Yt	Ti
Ti6Al4V, Cast (F 1108); Wrought (F 1472)								
≤0.05	≤0.1	≤0.015	≤0.30	≤0.20	5.5-6.75	3.5-4.5	≤0.005	Bal.
ELI, Wrought F136-13								
0.05	0.08	0.012	0.25	0.13	5.5-6.5	3.5-4.5	≤0.005	Bal.

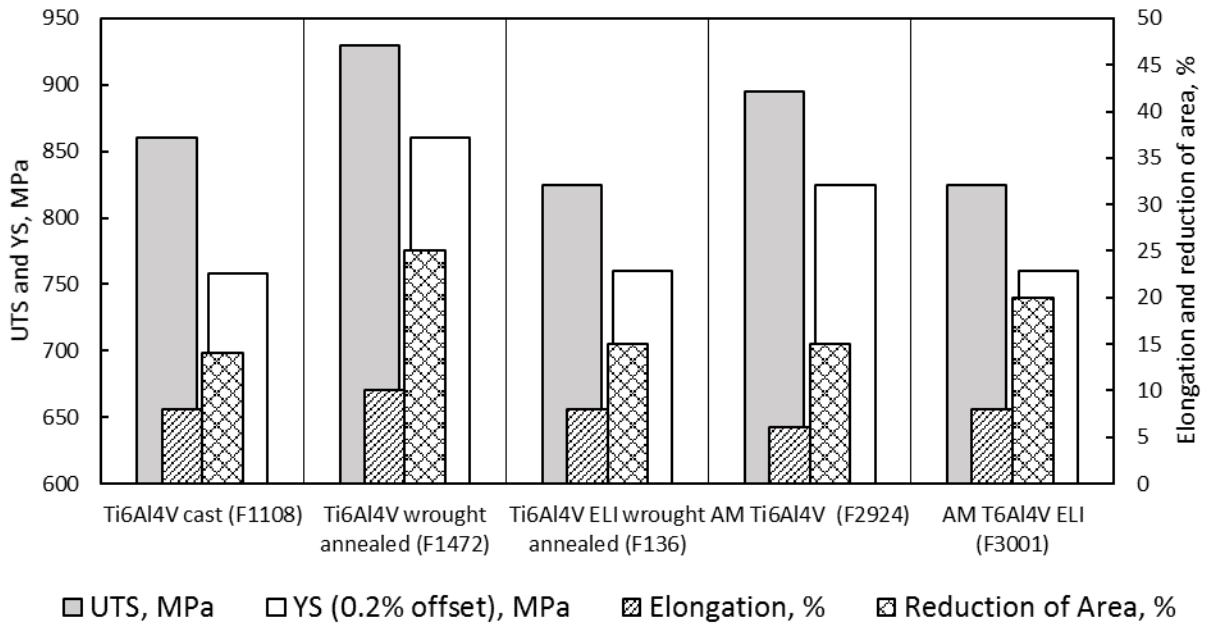

Figure 2. Minimum tensile properties for grade 5 (Ti6Al4V) and grade 23 (Ti6Al4V ELI) alloys for surgical implants in cast, wrought annealed states for surgical implants and material produced by powder bed fusion.

This investigation is dedicated to a systematic analysis of materials defects, microstructure and mechanical properties of LPBF Ti6Al4V ELI, making use of horizontal and vertical samples in as-built and heat treated conditions. The influence of heat treatment is an important issue for understanding of materials behavior and for development of new regimes for providing designed complex properties of LPBF materials.

Materials and methods

A chemical composition of the employed spherical argon-atomized Ti6Al4V ELI powders from TLS Technik GmbH & Co Spezialpulver KG is indicated in Table 2. The 10^{th}, 50^{th} and 90^{th} percentiles of equivalent diameter (weighted by volume) of the powder particles were d_{10}=11.2 μm, d_{50}=20.6 μm and d_{90}=31.8 μm for horizontal samples and d_{10} = 13 μm, d_{50}= 23 μm and d_{90} = 37 μm for vertical ones.

Table 2. Chemical composition of employed powders (wt. %)

	Ti	Al	V	O	N	H	Fe	C	Yt
Horizontal	Bal	6.44	3.99	0.12	<0.002	0.001	0.19	0.007	<0.001
Vertical		6.34	3.94	0.058	0.006	0.001	0.25	0.006	<0.001

Vertical and horizontal rectangular blocks were produced by the EOSINT M280 system with volume rate 5 mm³/s for 30 μm powder layer thickness. A back-and-forth (zigzag) scanning strategy by strips of 10 mm in width with the hatch distance of 100 μm was applied. All bars

10 mm×10 mm×60 mm in size were built without supports, directly on the substrates from Ti6Al4V. Argon was used as the protective atmosphere. The oxygen level in the chamber was controlled and it was in the range of 0.07–0.12%.

Tensile tests were performed with an Instron 1342 servo-hydraulic testing machine with clip-on extensometer of 12.5 mm and under strain rate of 0.5 mm/min and 1.5 mm/min after removal of the extensometer. Round specimens with threaded ends were machined from bars accordingly to the geometry recommended by ASTM E8M standard (gauge length four times the diameter). Three sets of specimens were manufactured. The first set of as-built bars were cut off from the substrates for further tests without heat treatment. The second and third sets of specimens remained on substrates were heat treated in Ar atmosphere at 650°C (Figure 3a) for stress relieving, then cut off. The third set was annealed in vacuum furnace at 950°C (Figure 3b).

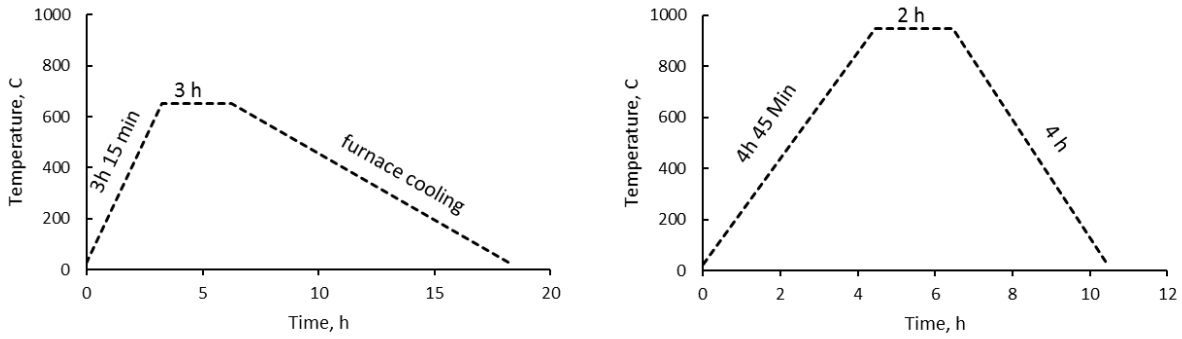

(a) (b)

Figure 3. Heat treatment procedures for stress relieving in Ar atmosphere (a) and annealing in vacuum furnace (b).

To investigate defects and porosity samples were subjected to X-ray micro computed tomography (microCT) with 10 μm resolution. The microCT scans were done at Stellenbosch CT facility (du Plessis *et al.*, 2016a) with a General Electric Phoenix V|Tome|X L240 system at 160 kV and 200 μA, including beam filtering of 0.5 mm copper. Reconstruction was done with system-supplied Datos software, making use of a strong beam hardening correction factor. Data analysis and 3D visualization was performed with Volume Graphics VGStudioMax 3.0. To simplify the analysis, 3D image processing was done using selection and morphological image operations to select the sample sub-surface by 50 μm in order to eliminate any edge noise effects. The defect analysis module was employed to perform an unbiased analysis of voids, using the same settings for all samples. In particular a minimum detected pore size of 30 μm was set, which corresponds to 3×3×3 voxels. The method is discussed in more detail in du Plessis *et al.* (2016b) where pores down to 4 μm could be detected. All microCT derived porosity in this work refers to pores >30 μm due to the sample size.

Results and discussion

Porosity

For the LPBF samples manufactured in horizontal direction, lack of fusion defects between tracks, stripes or islands can be critical in terms of ductility (Krakhmalev *et al.*, 2016). For the long

vertical samples, interlayer pores can play a role of stress concentrators and deteriorate mechanical properties (Beese *et al.*, 2016). The microCT scans showed that vertical and horizontal as-built LPBF samples had very low levels of porosity, the estimated porosities were 0.0004% and 0.0018% respectively). Maximum detected pore size was 205 μm (Table 3, Figure 4).

Table 3. Porosity of the samples from microCT scans

	Vertical, as-built	Vertical, stress-relieved	Horizontal, as-built	Horizontal, stress-relieved
Porosity, %	0.0004	0.0009	0.0018	0.0022
Number of pores	22	54	34	40
Maximum diameter of the pore, μm	96	137	132	205
Average diameter of the pores, μm	60±13.5	58±13.2	82±20	45±12
Maximum volume of the pore $\times 10^{-5}$ mm^3	9.5	11.1	26	7
Average volume of the pores $\times 10^{-5}$ mm^3	4.15±1.62	3.79+1.3	11.9±5.91	2±1.0
Minimum sphericity	0.57	0.6	0.54	0.43
Maximum sphericity	0.70	0.71	0.70	0.79
Average sphericity of the pores	0.65±0.035	0.65±0.036	0.62±0.028	0.71±0.06

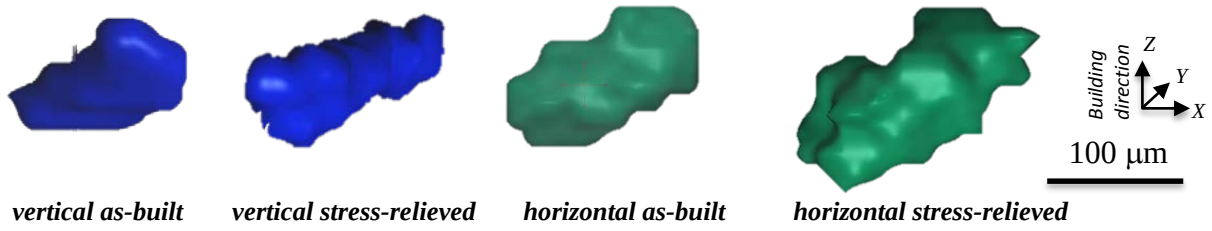

Figure 4. MicroCT reconstruction of the largest-pore shapes.

Figure 5 presents sphericity (that is the ratio of surface area of sphere with same volume as defect to the surface area of defect) and diameters of the defects *versus* position of the pores along sample's greatest dimension. Pores had different shapes, the biggest pores were more elongated. It should be noted that the pores were fairly randomly distributed along the long side of the samples both horizontal and vertical.

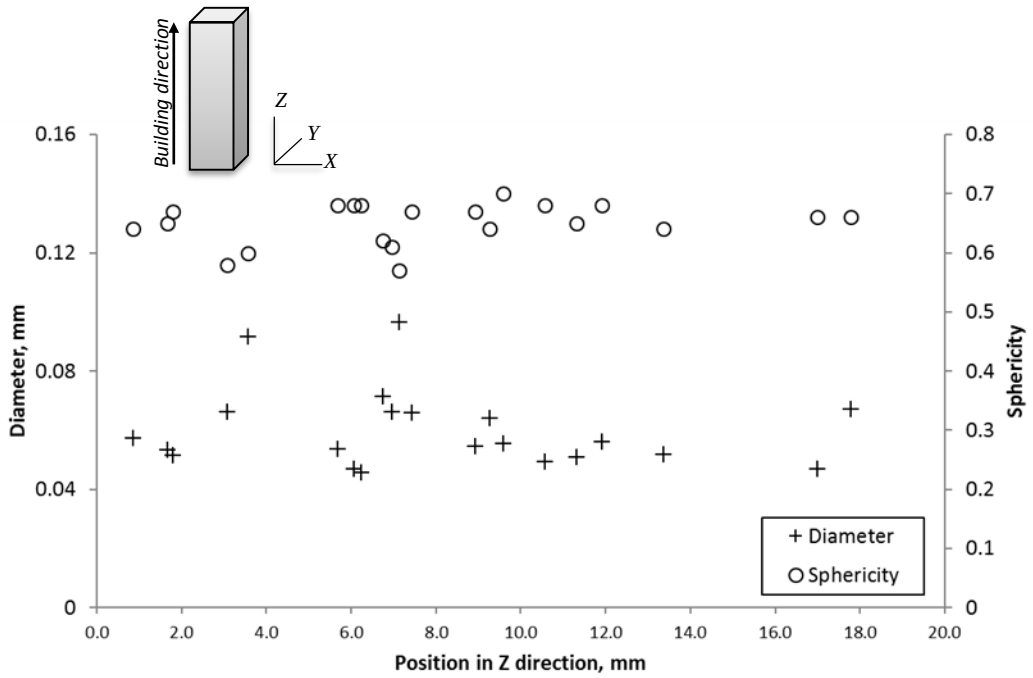

(a)

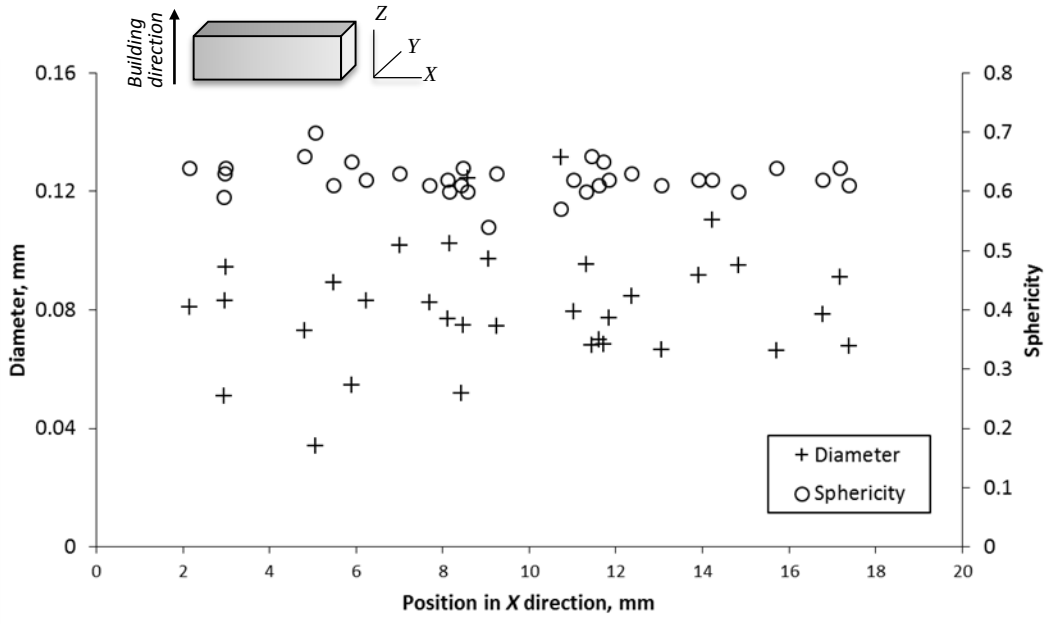

(b)

Figure 5. Diameters of the defects and sphericity in vertical (a) and horizontal (b) as-built samples.

Microstructure

At LPBF, material solidifies with high cooling rates (about 10^6 K/s), which results in formation of metastable structures of α´ hexagonal martensite with pronounced prior β-texturisation in building direction (Figure 6). As it was reported, although in LPBF Ti6Al4V alloy the β phase showed columnar growth with highly pronounced texture <100>, the texture of α´ needles was quite weak (Simonelli *et al.*, 2014). At present conditions, *in situ* decomposition of non-equilibrium phases did not occur in as-built LPBF samples. Also after stress relieving heat treatment, XRD and TEM analysis also confirmed needle-like structure without any β precipitations. Thermo-mechanical history of LPBF Ti6Al4V also caused presence of $\{10\bar{1}2\}$ type twins in the as-built and stress-relieved samples. This type of twins in *hcp* materials is often reported as tensile twins and observed twinning could be a possible mechanism for accommodation of thermal stresses during manufacturing (Krakhmalev *et al.*, 2016).

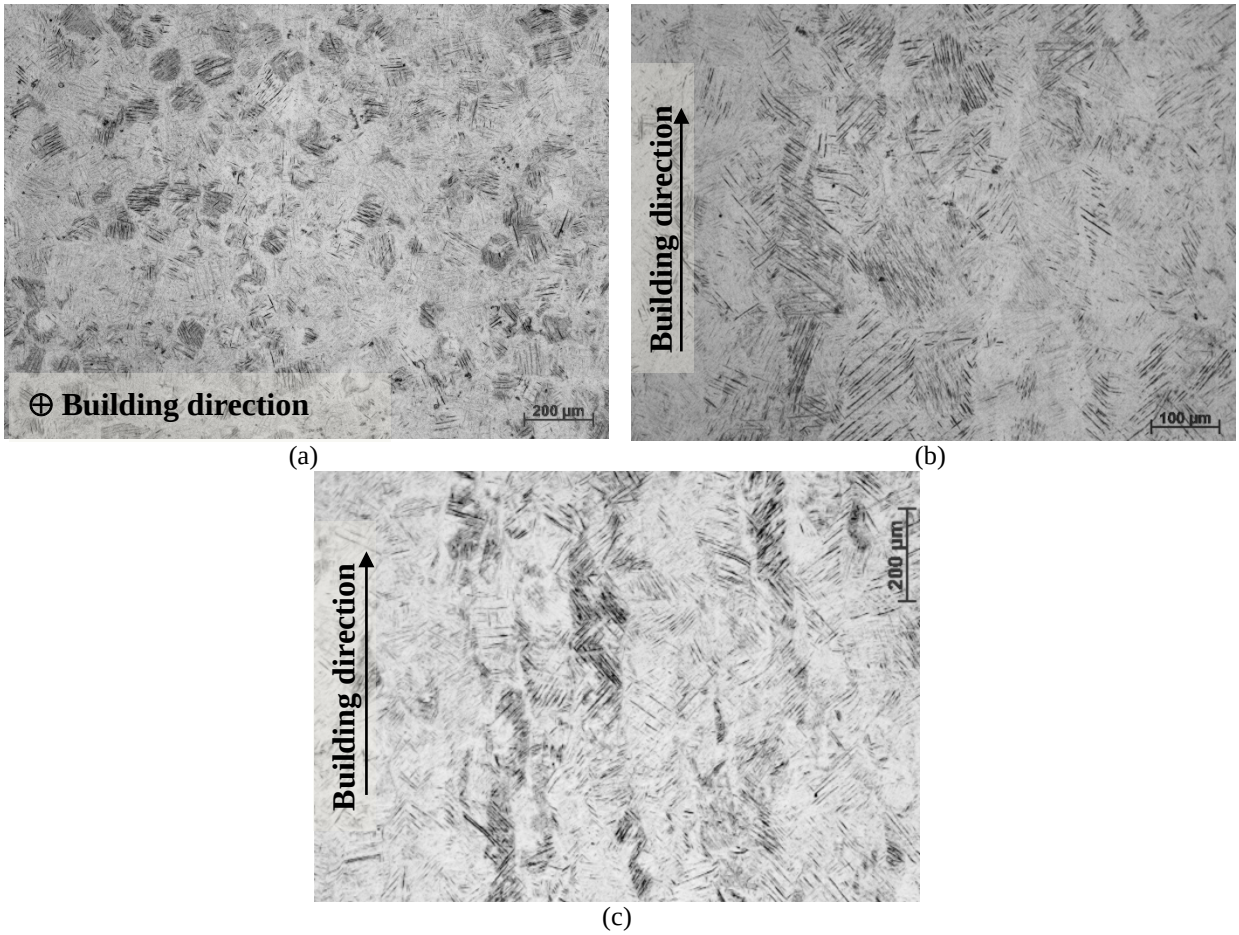

Figure 6. Microstructure of horizontal (a, b) and vertical (c) as-built samples at different cross-sections: perpendicular to the building direction (a) and along it (b, c).

The columnar boundaries of prior β-phase were still visible at the microstructure of horizontal and vertical LPBF samples. These boundaries were observed in as-built specimens and all specimens after heat treatments. In the specimens subjected to stress-relieving heat treatment

followed by annealing for 2 hours at 950°C (Figure 7a, c), they were also clearly visible although martensitic needle like microstructure was decomposed. Decomposition of the α′-martensite in Ti6Al4V, according to Mur *et al.* (1996) is accompanied with nucleation of fine α precipitates at martensite plate boundaries, enrichment of surroundings with β-stabilizers and finally, formation of the equilibrium α+β phases mixture. Nuclei of equiaxial α-phase were found in globular phase enriched by α-stabilizing Al and it was unevenly distributed in microstructure (Figure 7b and d). In the heat-treated specimens, there were no continuous alpha network at prior β-grain boundaries found. This type of microstructure corresponds exactly to standards for biomedical application required for annealed Ti6Al4V (ISO 20160, 2006).

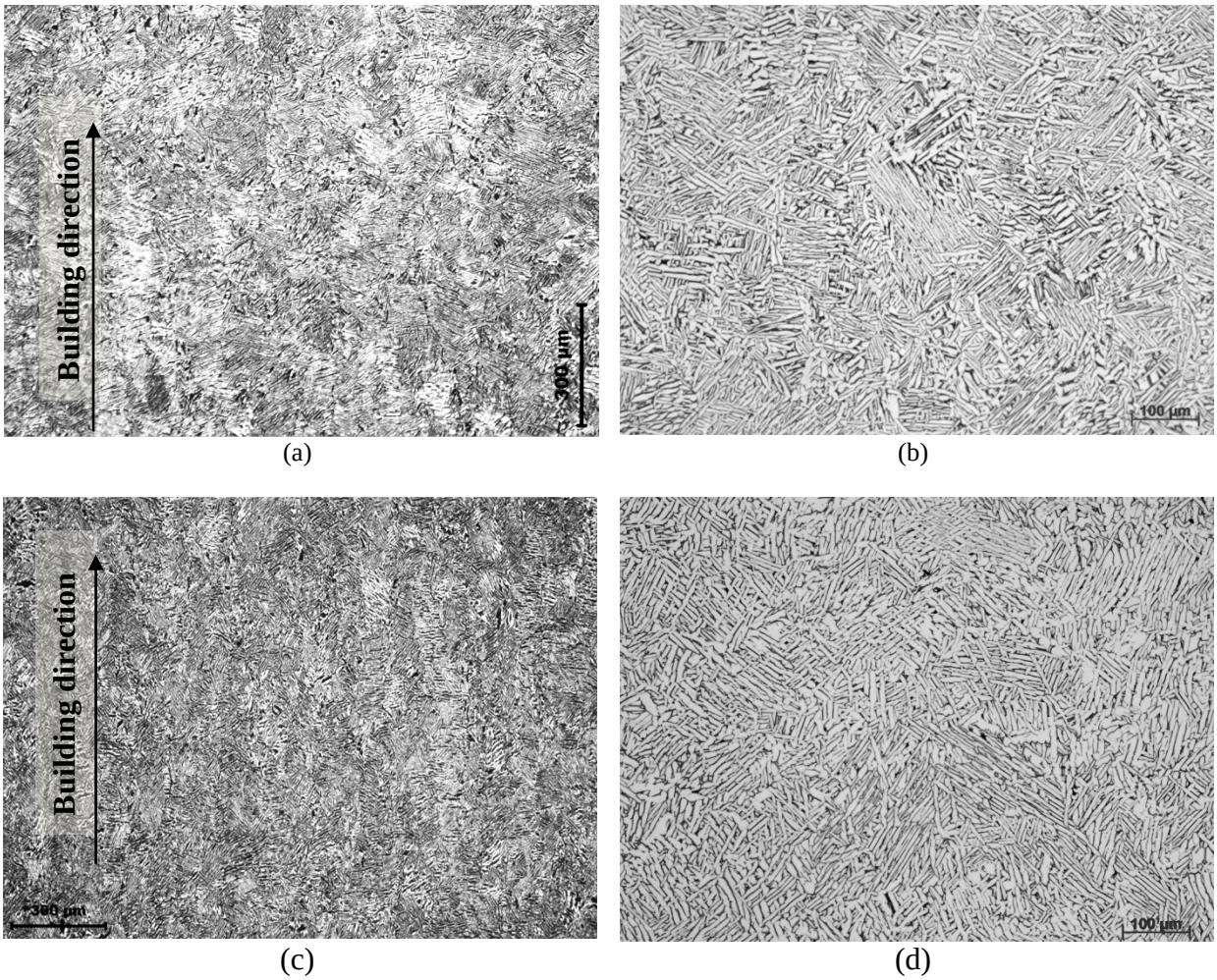

Figure 7. Microstructure of horizontal (a, b) and vertical (c, d) samples annealed at 950 °C.

Residual stress

Principal residual stresses were measured by XRD near the top surface in as-built Ti6Al4V LPBF cubes 10 mm×10 mm×10 mm, produced with similar process parameters and attached to the substrate. Residual stresses were tensile in nature and varied from 200 MPa to 800 MPa. These values were similar to the ones reported for cantilever specimens in as-built conditions. Van Zyl *et al.* (2016) reported that maximum residual stress was found to be 1100 MPa. A high variability of

residual stresses can be (at least partially) linked to the morphology of the processed layer and inhomogeneity of delivered powder layers which lead to different strains during cooling. The strain during cooling can be described as a superposition of elastic, thermal and plastic deformation, as well as creep strain components. The molten pool and the heat-affected zone had an elongated shape in the scanning direction. When the laser beam left the irradiated zone, the track solidified and cooled down. Various layers of material, cooled at different rates, therefore contraction also occurred at different speeds. During laser melting, high compressive and tensile stresses were under the front of the molten pool. As a result, deformations in the surrounding material and the solidifying track occurred. After stress relief heat treatment at 650°C for 3 hours, residual stress was about 30 MPa (Yadroitsava *et al.*, 2015).

Tensile properties

To investigate influence of heat treatment on mechanical characteristics of the specimens manufactured in horizontal and vertical direction and evaluate influence of heat treatment on basic mechanical properties, tensile tests were performed. Figure 8 shows the tensile mechanical properties of as-built, stress-relieved and annealed samples fabricated in the vertical and horizontal directions. Modulus of elasticity did not vary among them very much and was measured in a range of 110–119 GPa. The dispersion of data points in the tensile data around the mean was more pronounced in the horizontal samples. Repeatability of ultimate tensile strength in each series of experiments was very high, coefficients of variations were 0.2–0.9%. Reduction of area had the highest relative variability up to 9.4%.

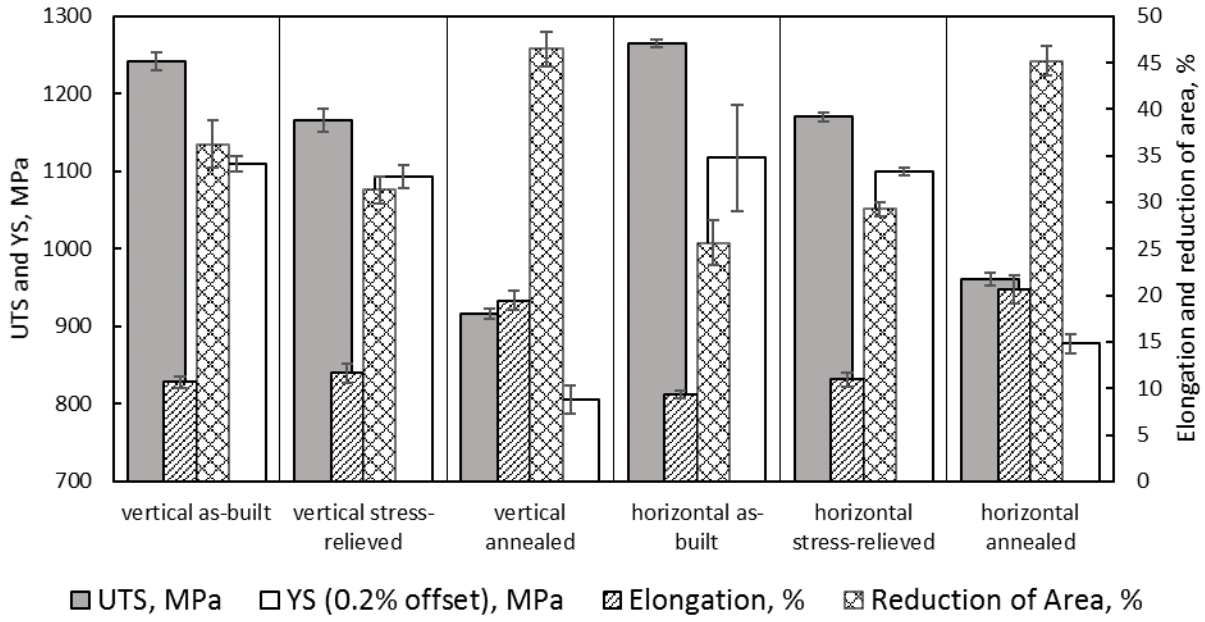

Figure 8. Tensile mechanical properties of vertical and horizontal samples.

The as-built samples had higher Ultimate Tensile Strength (UTS) compared to the stress-relieved and annealed specimens. Higher strength of the as-built samples, but rather lower ductility

were caused by residual stresses and fine martensitic structure. High strength characteristics are typical for as-built Ti6Al4V manufactured by LPBF (Rafi *et al.,* 2013; Vrancken *et al.,* 2014; Simonelli, 2014; Dimitrov *et al,* 2016; Krakhmalev *et al.,* 2016; Moletsane *et al.,* 2016). After 650 °C stress relief heat treatment, UTS decreased by 6–8% from the initial as-built level. A yield strength (YS) after stress-relieving heat treatment was not changed in comparison with as-built samples.

Annealing at 950 °C for 2 hours and followed by furnace cooling led to significant improvement in ductility of LPBF Ti6Al4V. This effect was observed in both horizontal and vertical series. Elongation at break was increased up to 20%, reduction of area reached values above 46% (Figure 8), and strength of LPBF Ti6Al4V ELI was even higher than required by standard specification for wrought alloy for surgical implant applications F136 (Figure 2). These changes in properties were the result of changes in microstructure and formation of microstructure close to equilibrium.

Fatigue properties

To investigate the influence of surface roughness, heat treatment and microstructure on the fatigue performance of Ti6Al4V ELI alloy manufactured by LPBF, a number of three-point bending fatigue tests were done at room temperature. The specimen was oriented so that the top or side surface was subjected to the highest tensile stresses, the other three surfaces were machined and grinded. As a reference, one series of as-built horizontal specimens was tested after machining and grinding of all surfaces (R_z~5 μm). The surface roughness of the samples *Rz* was measured with Surftest SJ-210 according to ISO 1997 standard.

The designations of specimens are presented in Table 4. Due to the limited numbers of specimens available, fatigue limit tests were not done, instead, fatigue life of materials was estimated at one maximum stress value of 700 MPa.

Table 4. The designation of specimens for fatigue testing

	Building direction	Tested surface	Surface roughness, *Rz*, μm	Conditions	Layers	Prior β-columns
H1A	Horizontal	Top	30–60	As-Built	Crack arrester	Parallel, along
H1B	Horizontal	Top		Stress-relieved	Crack arrester	Parallel, along
H2A	Horizontal	Side	120–135	As-Built	Crack divider	Parallel, across
H2B	Horizontal	Side		Stress-relieved	Crack divider	Parallel, across
V1A	Vertical	Side		As-Built	In plane	Perpendicular
V1B	Vertical	Side		Stress-relieved	In plane	Perpendicular
H1M	Horizontal	Top	5	As-built, grinded	Crack arrester	Parallel, along

Figure 9 presents logarithmic scale data on a number of cycles to failure. The results show some correlation of fatigue life with surface roughness. Higher roughness implies deeper valleys on the surface, which can be interpreted as notches. Stress concentration in notches lead to the

accelerated crack nucleation in the specimens with rougher surface. Highest roughness was measured on the side surface, and, accordingly, these specimens demonstrated shorter life to failure at 700 MPa. Top surface demonstrated slightly better performance, while machined specimens demonstrated the best performance and showed highest number of cycles to failure. Residual stresses substantially contribute in fatigue life. Among investigated specimens, stress relief resulted in an increase in numbers of cycles to failure in vertically manufactured specimens. In the horizontally manufactured specimens the effect was opposite and specimens after stress relief showed shorter number of cycles to failure. This effect is difficult to explain. On the top surface, commonly, tensile stresses were reported. Relief of tensile stresses should in principle influence fatigue life positively. The observed decrease in a number of cycles to failure could be a result of complex distribution of stresses on the surface. The effect, nevertheless, is needed to be confirmed with more statistical investigations at different maximum stress values.

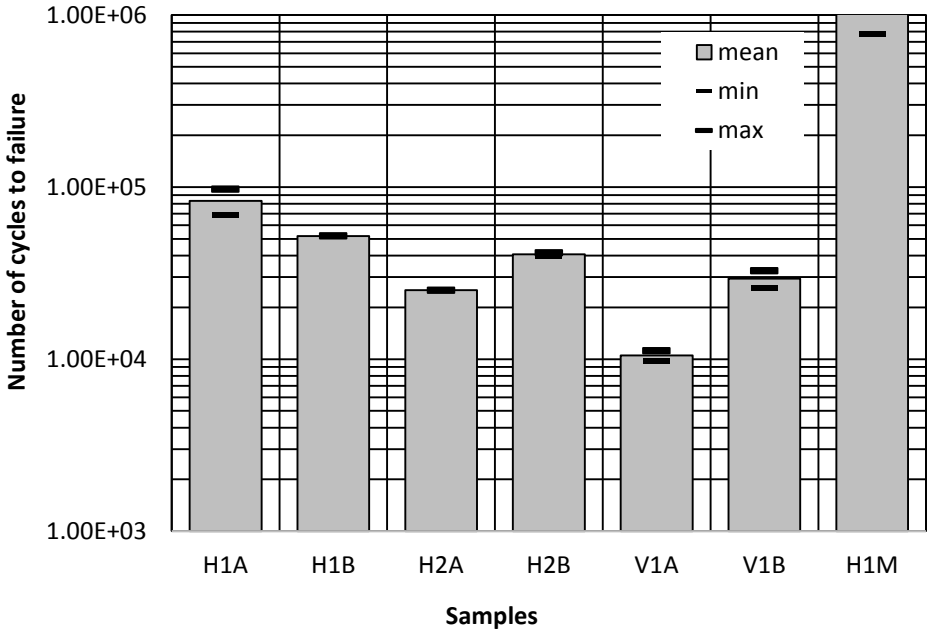

Figure 9. Cycles to failure of the LPBF Ti6Al4V ELI specimens at 700 MPa maximum stress. Designation of the samples are shown in Table 4.

Crack propagation rate was investigated based on electron microscopy observations of striations on the fracture surfaces. Fatigue crack propagation criteria, or Paris law, was used for estimation crack growth rate *da/dN*

$$\frac{da}{dN} = c\Delta K^m \qquad \text{(Eq. 1)},$$

where *a* is the crack length, *N* is the number of cycles, *c* and *m* values are the material parameters, ΔK is the stress intensity range.

Typically for the *da/dN* data of LPBF Ti6Al4V alloy, remarkable spread of data and somewhat erratic behavior (Edwards and Ramulu, 2015; Leuders *et al.*, 2013) were observed. Due to that, threshold values ΔK_{th} were difficult to extrapolate and could be estimated about 10 MPam^{½}, and critical values of ΔK_{IC} were in range 39-45 MPam^{½}. Linear parts of the *da/dN versus* ΔK curves are presented in Figure 10, parameters of Paris law summarized in Table 5.

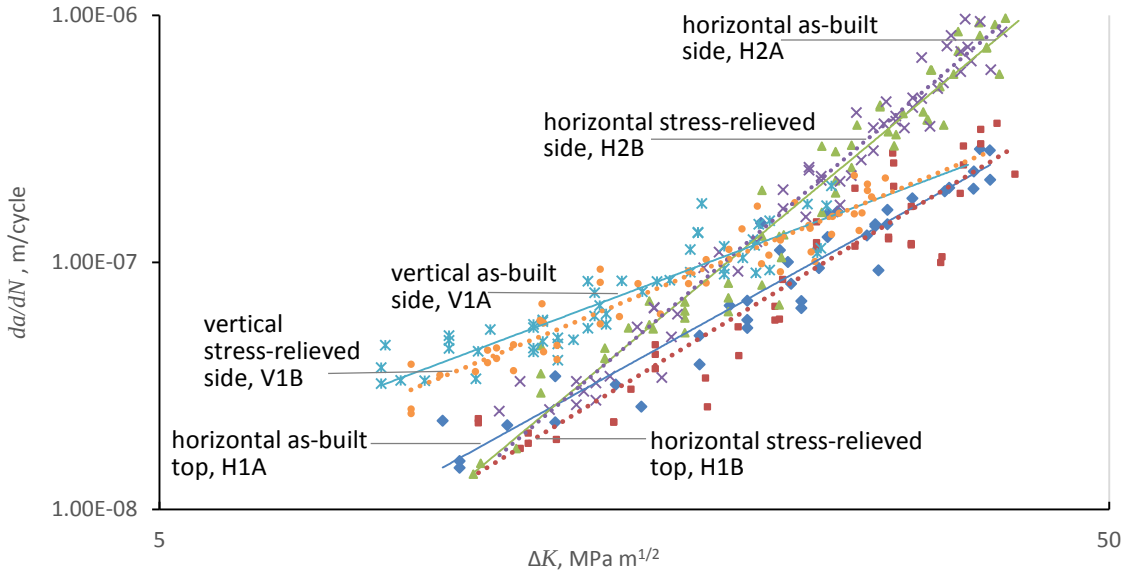

Figure 10. Fatigue crack propagation rate of different LPBF samples.

Table 5. Fatigue testing results*

Sample		*C*	*m*
H1A	Horizontal as-built	1.12×10^{-10}	2.13
H1B	Horizontal stress-relieved	5.37×10^{-11}	2.34
H2A	Horizontal as-built	7.31×10^{-12}	3.19
H2B	Horizontal stress-relieved	5.38×10^{-12}	3.3
V1A	Vertical as-built	1.43×10^{-9}	1.45
V1B	Vertical stress-relieved	9.12×10^{-10}	1.58

* See (Eq. 1)

To some extent these values are in agreement with Paris law parameters reported by other investigators for LPBF Ti6Al4V (Edwards and Ramulu, 2015; Leuders *et al.*, 2013; Dhansay *et al.*, 2014). Nevertheless, unlike that reported by Edwards and Ramulu (2015) and Dhansay *et al.* (2014), crack penetration behavior was found to be dependent on the specimen orientation. Influence of residual stresses on crack propagation behavior, according to the data obtained in this study, was not very high. It was observed that parameters for materials manufactured with the same orientation in as-built and stress-relieved conditions vary insignificantly. Bigger differences were observed between specimens manufactured in different directions.

Specimens manufactured horizontally but tested with the highest stresses at the side surface showed the steepest slope of the linear part of *da/dN* curve compared to horizontal tested at the top surface, and vertically manufactured specimens. Differences in crack propagation rate could be explained by interaction of the crack with microstructural features and interfaces in the LPBF material. Table 4 summarizes orientation of crack and microstructural features in different specimens. In a case of specimens tested at the top surface and manufactured horizontally, layers have crack arrester orientation. Interaction of a crack with internal interfaces therefore can result in crack deviation, thus decreasing crack propagation rate. In specimens manufactured horizontally but tested at the side surface, layers have a crack divider orientation. Experimental observations demonstrated that layers having crack arrester orientation resist crack growth more efficiently. The lowest *m* value, and therefore the lowest crack propagation rate, was observed for vertically manufactured specimen (Table 5), where interlayer interfaces were in plane with crack growth direction (Figure 10), which was an unexpected result.

This behavior could be explained assuming that column boundaries of prior β-phase also resist crack propagation. In the horizontally manufactured specimens, resistance of these boundaries is not very high as the crack grows along boundaries. Therefore, interlayer boundaries are more important in specimens tested with this orientation. In vertically manufactured specimens, crack penetrates perpendicularly to the boundaries of columnar prior β-grains. In these specimens the *m* value is the lowest i.e. crack propagation rate is also low. Nevertheless, these specimens showed lowest number of cycles to failure, and observed crack before final failure occurred was shorter compared to the horizontally manufactured specimens. It means that although, prior β-grain boundaries seem to be quite efficient in resistance to fatigue crack propagation the material has lowest fatigue life, likely due to high surface roughness.

Fracture surface analysis

The fracture surfaces after tensile tests of specimens in as-built, stress-relieved and annealed conditions had cup-and-cone shapes and obvious necking. In the annealed samples, necking was more pronounced. Necking is commonly associated with ductile fracture. The central area, commonly described as a region of fibrous fracture, was clearly distinguished apart from the shear lips on the periphery. The fractured surface in the fibrous zone was irregular (Figure 11). Electron microscopy analysis revealed a formation of dimples, suggesting dimpled rupture fracture in the fibrous zone. Although the dimpled rupture was dominating, quasi-cleavage facets were observed in as-built and stress-relieved samples. High-magnification analysis showed that martensite needles were visible on the quasi-cleavage surfaces in as-built and stress-relieved samples (Figure 11a, b). Therefore, it is possible to confirm that these regions are formed when the crack propagates along a martensite colony. When the crack reaches a primary β-grain boundary or a fusion boundary, the growth direction is changed. The interface, therefore, acts as a crack deflector preventing quick failure. This conclusion is in agreement with results presented by Wen *et al.* (2014). In annealed samples features of brittle fracture like quasi-cleavage surfaces were not found. The dimples from inner fracture zone were more pronounced, with bigger size and shapes elongated in the direction of the load (Figure 11).

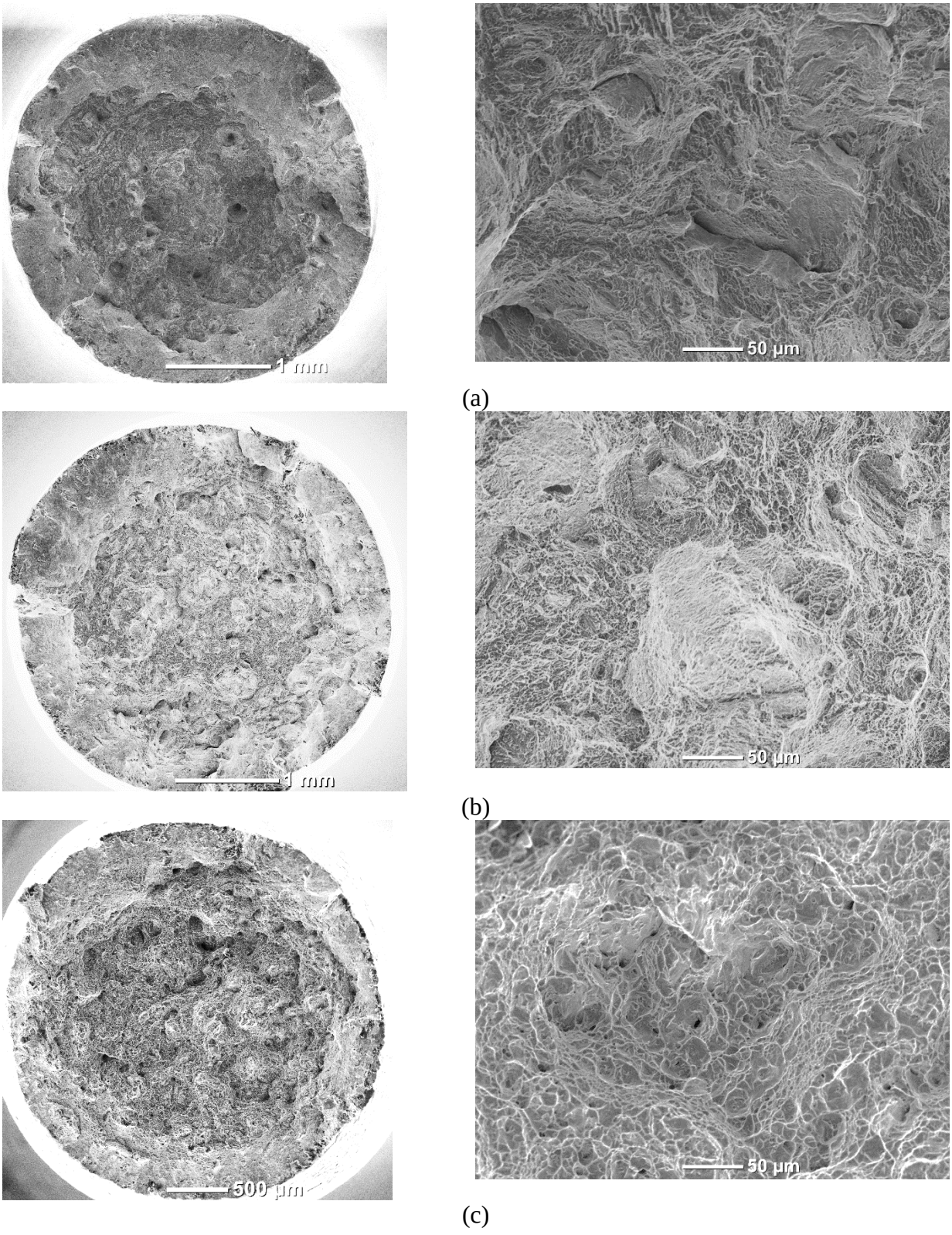

Figure 11. SEM photos of the fracture surfaces of horizontal as-built (a), vertical stress-relieved (b) and annealed samples (c).

Cup-and-cone morphology is typical for fracture controlled by pore coalescence mechanisms. A process of pore formation and coalescence was investigated by means of micro computed tomography. The as-built and stress-relieved specimens were pre-strained to 1.57–9.44%, the pore sizes were investigated. CT scans showed coalescence of the pores under loading in the pre-strained samples, pores looked like an agglomerate of several pores (Figure 12a). Some pores were interconnected with quite thin channels, possibly the initial stages in formation of cracks or new pores.

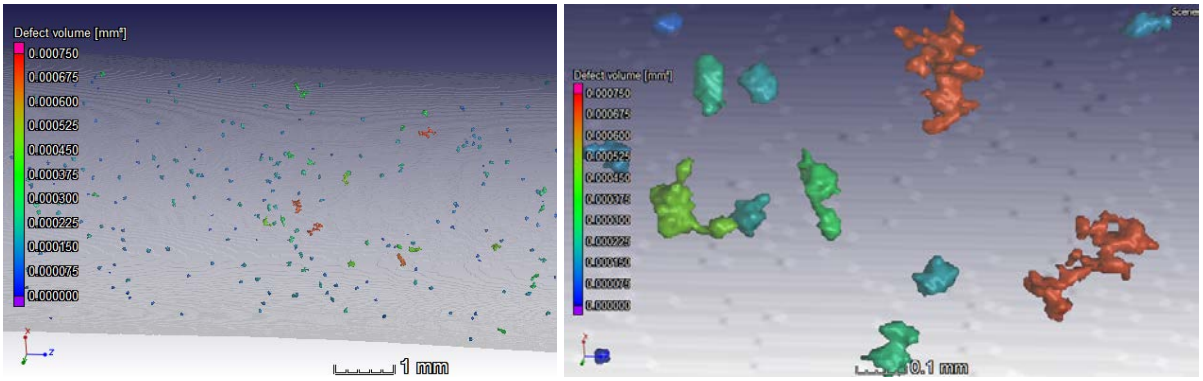

(a)

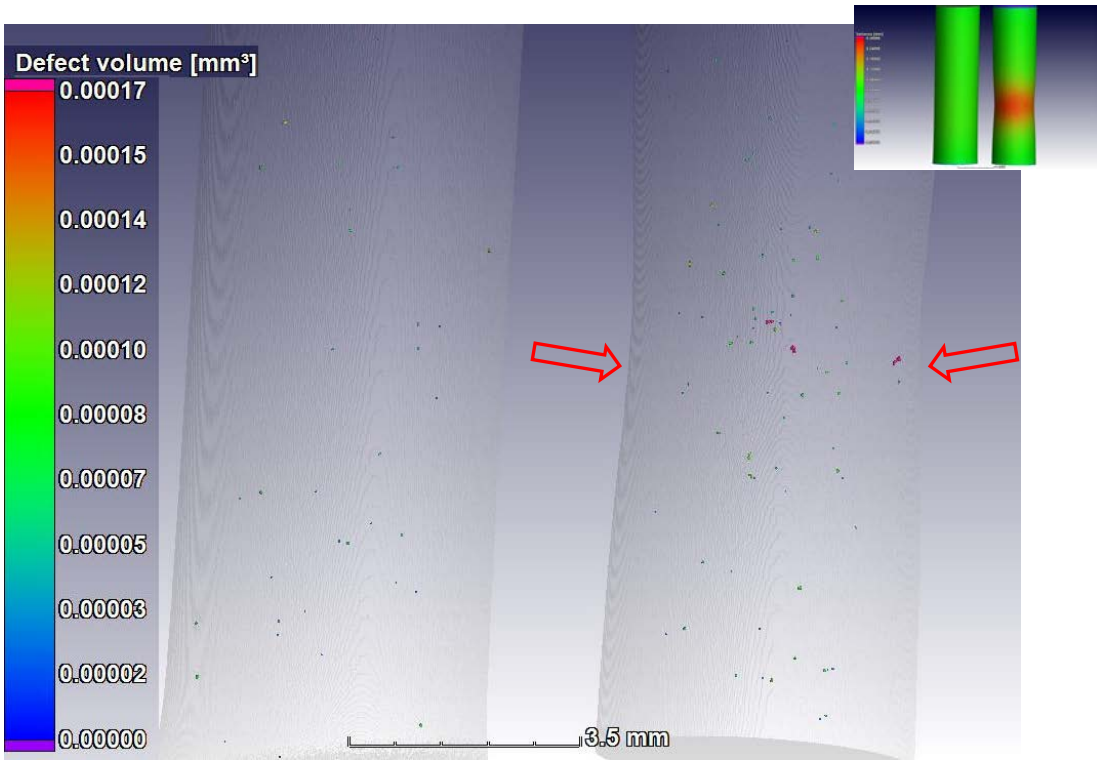

Figure 12. Reconstruction of porosity in as-built sample deformed to 8.2% from the initial length (a) and necking creation in stress-relieved sample deformed from 3.55% to 9.44% from initial length (b). Defect analysis shows colour coded porosity distribution in transparent 3D views. The insert shows a colour coded thickness variation, indicating clearly the necking region.

As the specimen was strained, pore coarsening was clearly pronounced and was dominating in the necking area (Figure 12b). The number of pores identified by CT scans significantly increased in this region. Analysis of cumulative frequency distributions of equivalent pore diameters in pre-strained, as-built and stress-relieved samples showed that pores became bigger with strains. Most of new pores were observed in the neck region and they could be a nucleation point of the crack leading to the final failure (Krakhmalev *et al.*, 2016; Moletsane *et al.*, 2016).

Influence of the microstructure on the fracture mode

To observe influence of building direction, i.e. microstructure and orientation of prior β-grains on mechanical behaviour of the LPBF Ti6Al4V, longitudinal cross-sections of broken samples were investigated. In the horizontal specimens two cross sections were made, one along and one across the building direction. In all specimens, narrowing and elongation of prior β-grains was observed in the neck region.

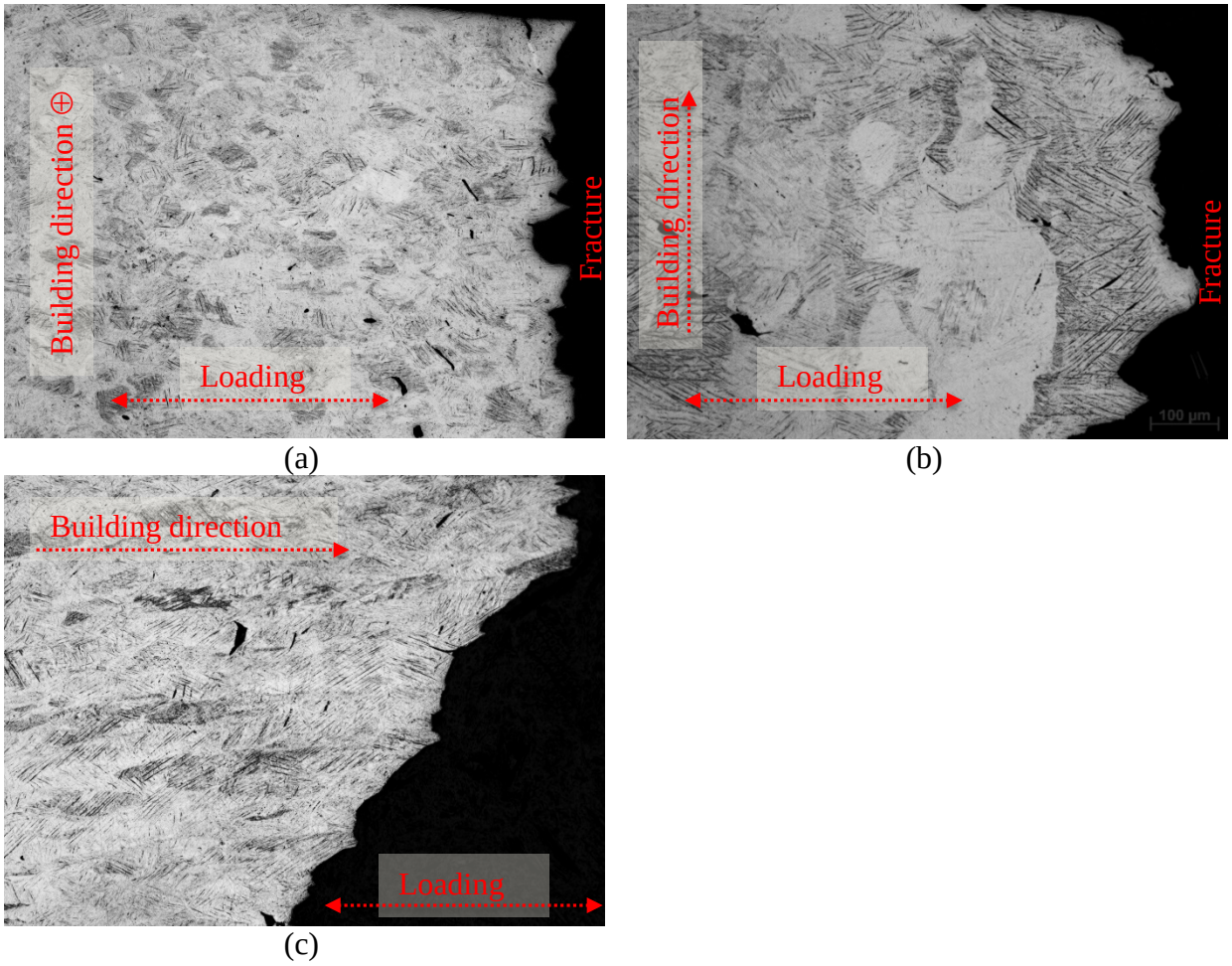

Figure 13. Microstructure of horizontal (a, b) and vertical (c) as-built samples after tensile tests at different cross-sections: perpendicular to the building direction (a) and along it (b, c).

In the horizontal specimens, tested perpendicular to the building direction, crack penetration could be sensitive to the microstructure due to structural anisotropy. In Figure 13a, the

broken specimen was cut perpendicular to the building direction, in Figure 13b the cut plane was oriented parallel to the building direction. It is seen that in Figure 13a, crack grew rather in the inter-granular mode, following the boundaries of prior β-columns and inter-granular crack propagation is the dominating mechanism. In Fig. 13b crack propagates along the boundaries of prior β-columns and also through the columnar grains, apparently parallel to the lamella visible in the microstructure. Presence of the mixed fracture mode could explain experimental observations of quasi-cleavage and dimpled fracture modes mutually. In the vertical specimens, only intra-granular fracture was observed in the cross-sections (Figure 13c).

As indicated by Simonelli (2014), grain boundaries are the weak points in the microstructure where cracks can propagate easier. Apparently, presence of long prior β-grain boundaries perpendicular to the loading direction could be a reason for the lower ductility experimentally observed in the horizontal specimen.

After the stress relieving heat treatment, there were no differences in mechanical properties of among vertical and horizontal samples. The mixed fracture mode was observed in horizontally manufactured specimens (Figure 14a) similar to as-built samples. Narrowing and elongation of prior β-grains in stress-relieved vertical samples under tensile loading is presented in Figure 14b.

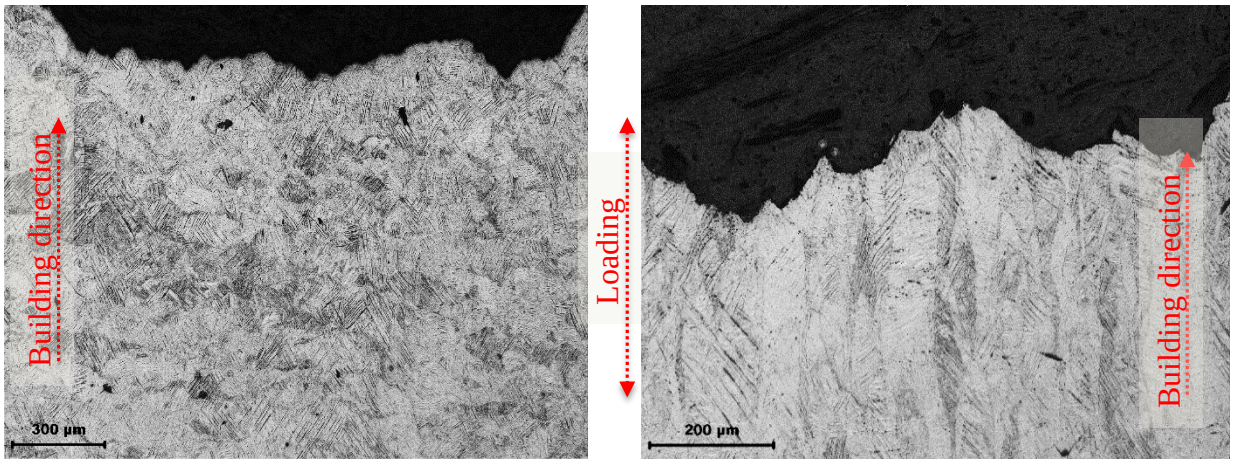

(a) (b)

Figure 14. Microstructure after tensile tests of stress relieve horizontal (a) and vertical samples (b) at cross-section parallel to the building direction.

Heat treatment for 2 hours at 950°C lead to changes in the microstructure and properties. Martensitic needle-like structure transformed to alpha phase lamella with some beta phase, Figure 15. Only very small (~0.5 μm) globular grains of the alpha phase were found after stress-relieving heat treatment (Krakhmalev *et al.*, 2016). Notable, that after this heat treatment, prior β-phase columns boundaries are still recognizable in the microstructure. After loading of heat-treated specimens, no indication of brittleness was observed at fracture surface, grains were well plastically deformed (Figure 15). Fracture surface analysis allowed to suppose that crack propagating happened along alpha lamella or α-β interfaces. Influence of prior β-grain boundaries was not that strong as it was observed in horizontal as-built specimens.

Observation of cross sections near the neck region in as-built specimens and after all selected heat treatments revealed that nucleation and coalescence of pores was the main mechanism governing the failure under tension. Pores that were observed in the as-built and stress relived materials were elongated and mostly located between α′ martensite needles or on colony boundaries (Figure 13 and Figure 14). Stress relieve did not change pore nucleation sites and, therefore, it is possible to conclude that pore coalescence is related to anisotropy in the microstructure. In the materials heat treated for 2 hours at 950°C, a similar situation was observed. Pores nucleated at α lamella boundaries and grew under the tension (Figure 15). These microscopy observations were in very good agreement to the microCT investigations described above. Interestingly, it was not the pores existing in the materials after manufacturing that resulted in the final failure, rather new pores nucleated, grew and coalesced to create the final crack that led to the failure.

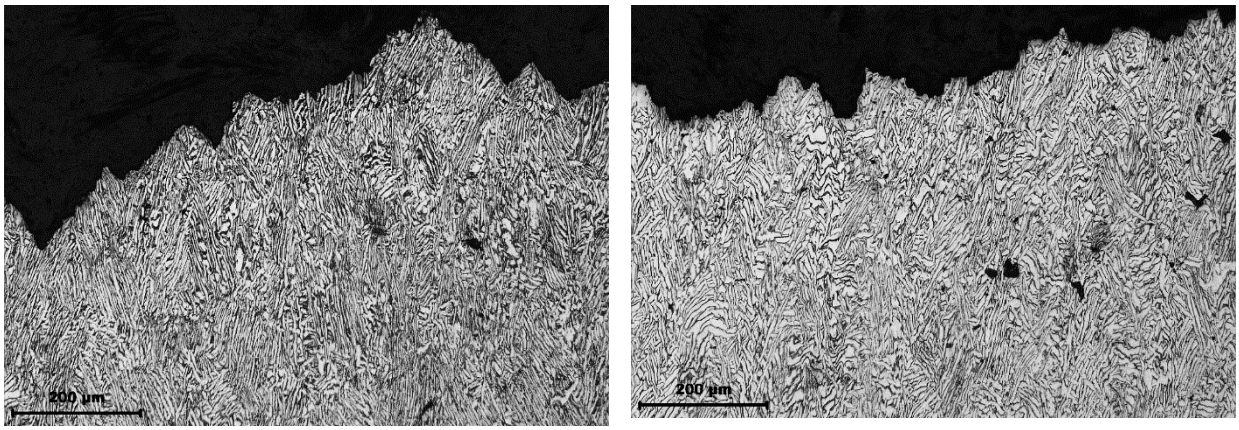

(a) (b)

Figure 15. Cross-section of the fractures in horizontal (a) and vertical (b) samples annealed at 950 °C.

Conclusions

By LPBF, high density can be achieved at optimal process parameters and scanning strategy. In the presented study, for Ti6Al4V ELI samples the density measured by microCT scans, was higher than 99.99% (for pores >30 µm). The typical pore size in the as-built material was in a range of 30-200 µm. MicroCT scans and cross-sectioning microscopic analysis showed that the biggest pores were predominantly elongated in shape and could be considered as interlayer pores.

LPBF manufacturing led to high residual stresses in as-built objects and unique microstructure due to high cooling rates. Ti6Al4V ELI as-built microstructure consists of hexagonal α' martensitic needles. No beta βprecipitations were found in the as-built samples or after stress relief heat treatment at 650°C for 3 hours. Annealing at 950°C for 2 hours decomposed α' martensite and transformed microstructure to $\alpha+\beta$ phases mixture with few α phase equiaxial small grains randomly distributed in the volume.

As-built samples fabricated in vertical and horizontal directions showed high strength and relatively low ductility about 10% caused by presence of residual stresses and very fine martensitic

structure. After stress relief heat treatment, UTS decreased by 6–8% and YTS was not changed. Annealing led to significant improvement in ductility, elongation of break was increased up to 20%. The modulus of elasticity varied insignificantly and it was in a range of 110-119 GPa.

Investigations of development of the porosity in as-built and heat treated samples under interrupted tensile test conditions revealed that nucleation and coalescence of new pores instead of growth of existing pores in the necking region, was the main mechanism causing fracture.

The crack propagation rate was found dependent on the specimen orientation and insignificantly dependent on residual stresses. Bending fatigue properties of horizontal specimens showed correlation of a number of cycles to failure with surface roughness. The specimens with rougher surface demonstrated decreased number of cycles to failure.

Cup-and-cone shaped fracture was observed in specimens in as-built and heat treated conditions. Nevertheless, mixed fracture mode with features of ductile dimpled rapture and brittle quasi-cleavage surfaces was found in as-built and stress-relieved samples. In annealed condition, fracture mode was ductile.

Analysis of influence of the microstructure on the fracture modes showed that in horizontal specimens inter-granular (along prior β-grain boundaries) and intra-granular (along lamella in a colony) fractures occurred. In vertical samples only intra-granular type of the fracture was found. Weak prior β-grain boundaries initiating inter-granular fracture, therefore, could be a reason for decreased ductility observed at tension tests of horizontal specimens.

This study showed that the LPBF Ti6Al4V ELI has a specific microstructure and mechanical properties, which are comparable to or even superior to those of the conventional material. Thus, there is a clear need to accelerate the development of new standards that would give clear quality indicators for this type of materials for biomedical applications.

Acknowledgements

This work is based on the research supported by the South African Research Chairs Initiative of the Department of Science and Technology and National Research Foundation of South Africa (Grant №97994) and the Collaborative Program in Additive Manufacturing (Contract №CSIR-NLC-CPAM-15-MOA-CUT-01). Mechanical testing has been performed in mechanical testing laboratory in CSIR and authors are grateful to Chris McDuling.

References

ASTM F1108–14. *Standard Specification for Titanium-6Aluminum-4Vanadium Alloy Castings for Surgical Implants* (UNS R56406). STM International, West Conshohocken, PA, 2014.

ASTM F136–13. *Standard Specification for Wrought Titanium-6Aluminum-4Vanadium ELI (Extra Low Interstitial) Alloy for Surgical Implant Applications* (UNS R56401). ASTM International, West Conshohocken, PA, 2013.

ASTM F1472–08. *Standard Specification for Wrought Titanium-6Aluminum-4Vanadium Alloy for Surgical Implant Applications* (UNS R56400). ASTM International, West Conshohocken, PA, 2008.

ASTM F2924–14. *Standard Specification for Additive Manufacturing Titanium-6 Aluminum-4 Vanadium with Powder Bed Fusion.* ASTM International, West Conshohocken, PA, 2014.

ASTM F3001–14. *Standard Specification for Additive Manufacturing Titanium-6 Aluminum-4 Vanadium ELI (Extra Low Interstitial) with Powder Bed Fusion*. ASTM International, West Conshohocken, PA, 2014.

ASTM F620–11. *Standard Specification for Titanium Alloy Forgings for Surgical Implants in the Alpha Plus Beta Condition*. ASTM International, West Conshohocken, PA, 2015.

ISO 20160:2006. *Implants for surgery. Metallic materials – Classification of microstructures for alpha+beta titanium alloy bars.*

Dhansay N.M., Tait, R. Becker T., 2014. Fatigue and fracture toughness of Ti-6Al-4V titanium alloy manufactured by Selective Laser Melting. *Advanced Materials Research*, 1019, pp. 248-253.

Dimitrov, D., Becker, T.H., Yadroitsev, I., Booysen, J., 2016. On the impact of different system strategies on the material performance of selective laser melting-manufactured TI6AL4V components. *The South African Journal of Industrial Engineering*, 27(3), pp. 184–191.

du Plessis, A., le Roux, S.G., Guelpa, A., 2016a. The CT Scanner Facility at Stellenbosch University: An open access X-ray computed tomography laboratory. *Nuclear Instruments and Methods in Physics Research Section B: Beam Interactions with Materials and Atoms*, 384, pp. 42-49.

du Plessis, A., le Roux, S.G., Booysen, G., Els, J., 2016b. Quality Control of a Laser Additive Manufactured Medical Implant by X-Ray Tomography. *3D Printing and Additive Manufacturing*, 3(3), pp. 175-182.

Edwards, P., Ramulu, M., 2015. Effect of build direction on the fracture toughness and fatigue crack growth in selective laser melted Ti-6Al-4 V. *Fatigue Fract. Engng. Mater. Struct*, 38, pp. 1228–1236.

Kasperovich, G., Hausmann, J., 2015. Improvement of fatigue resistance and ductility of TiAl6V4 processed by selective laser melting. *Journal of Materials Processing Technology*, 220, pp. 202–214.

Krakhmalev, P., Fredriksson, G., Yadroitsava I., Kazantseva N., du Plessis, A., Yadroitsev, I., 2016. Deformation behavior and microstructure of Ti6Al4V manufactured by SLM. *Physics Procedia*, 83, pp. 778 – 788.

Leuders S., Thöne M., Riemer A., Niendorf T., Tröster T., Richard H.A., Maier H.J., 2013. On the mechanical behaviour of titanium alloy TiAl6V4 manufactured by selective laser melting: Fatigue resistance and crack growth performance. *International Journal of Fatigue*, 48, pp. 300-307.

Moletsane, M.G., Krakhmalev, P., Kazantseva, N., du Plessis, A., Yadroitsava, I., Yadroitsev, I., 2016. Tensile properties and microstructure of direct metal laser-sintered Ti6Al4V (ELI) alloy. *The South African Journal of Industrial Engineering*, 27(3), pp. 110-121.

Mur F.X.G., Rodriguez D., Planell, J.A., 1996. Influence of tempering temperature and time on the α'-Ti-6Al-4V martensite. *Journal of Alloys and Compounds*, 234, pp. 287–289.

Rafi, H.K., Karthik, N.V., Gong, H., Starr, T.L. Stucker, B.E., 2013. Microstructures and mechanical properties of Ti6Al4V parts fabricated by selective laser melting and electron beam melting. *Journal of Materials Engineering and Performance*, 22(12), pp. 3873-3883.

Simonelli, M., 2014. *Microstructure evolution and mechanical properties of selective laser melted Ti-6Al-4V*, PhD thesis, Loughborough University, UK.

Van Zyl I., Yadroitsava I., Yadroitsev I., 2016. Residual stress in Ti6Al4V objects produced by direct metal laser sintering. *The South African Journal of Industrial Engineering*, 27(4), pp. 134-141.

Vrancken, B., Cain, V., Knutsen, R., Van Humbeeck, J., 2014. Residual stress via the contour method in compact tension specimens produced via selective laser melting. *Scripta Materialia*, 87, pp. 29–32.

Wen, S., Li, S., Wei, Q., Yan, C., Zhang, S., Shi, Y., 2014. Effect of molten pool boundaries on the mechanical properties of selective laser melting parts. *Journal of Materials Processing Technology*, 214, pp. 2660-2667.

Yadroitsava I., Grewar S., Hattingh D., Yadroitsev I., 2015. Residual stress in SLM Ti6Al4V alloy specimens. *Materials Science Forum*, 828-829, pp. 305-310.

Yadroitsev, I., Krakhmalev, P. Yadroitsava, I., 2015. Hierarchical design principles of selective laser melting for high quality metallic objects. *Additive Manufacturing J.*, 7, pp. 45–56.